Materials Science & Engineering R 165 (2025) 101003

Contents lists available at ScienceDirect

Materials Science & Engineering R

journal homepage: www.elsevier.com/locate/mser

Sterilizable vertical n-type organic electrochemical transistors for skin-conformal ECG monitoring

Ji Hwan Kim [a,1,2], Inho Lee [b,1], Won-June Lee [c,1], Dongjoon Shin [d], Hyeongbeom Lee [b], Lucas Q. Flagg [e], Jagrity Chaudhary [c], Liyan You [c], Keehoon Kang [a,*], Jianguo Mei [c,*], Sungjun Park [b,d,**]

[a] Department of Materials Science, Seoul National University, Seoul 08826, Republic of Korea
[b] Department of Intelligence Semiconductor, Ajou University, Suwon 16499, Republic of Korea
[c] James Tarpo Jr. and Margaret Tarpo Department of Chemistry, Purdue University, West Lafayette, IN 47907, USA
[d] Department of Electrical and Computer Engineering, Ajou University, Suwon 16499, Republic of Korea
[e] Materials Science and Engineering Division, National Institute of Standards and Technology, Gaithersburg, MD 20899, USA

ARTICLE INFO

Keywords:
Organic electrochemical transistor
Organic mixed ionic–electronic conductor
n-doped poly(benzodifurandione)
Vertically integrated device
Durable electrocardiogram sensor

ABSTRACT

The development of stable, high-performance epidermal biosignal monitoring devices is critical for advancing wearable healthcare technologies. Here, we present a novel electrochemical transistor-based biosignal sensor utilizing a 4-terminal vertical Corbino configuration and an n-doped poly(benzodifurandione) (n-PBDF) polymer. The 4-terminal device configuration effectively reduces the parasitic resistance, enabling a high transconductance of 374 mS at a low operational voltage, and one of the highest reported μC^* values of 1787 F cm^{-1} V^{-1} s^{-1} for *n*-type OECTs. In addition, this device achieves exceptional operational stability, maintaining consistent performance over extended periods, and demonstrates a superior shelf-life stability under ambient conditions. Furthermore, the sensor exhibits robust sterilization capabilities, withstanding both UV and thermal sterilization processes without performance degradation. Mechanical flexibility, a key requirement for on-skin applications, is ensured by the intrinsic properties of the n-PBDF polymer and the ultra-thin device architecture. The combination of these features makes this device an ideal candidate for monitoring of biosignals such as electrocardiograms, addressing practical challenges in wearable biosensing technologies.

1. Introduction

Organic electrochemical transistors (OECTs), which utilize organic mixed ionic–electronic conductors (OMIECs), have gained significant attention in bioelectronics due to their high transconductance (g_m), operational stability, and low-noise biosignal transduction, positioning them as a promising platform for advanced healthcare technologies [1–3]. Despite remarkable performance and response speed advancements enabled by novel OMIECs, research has predominantly centered on device metrics, often neglecting the broader requirements for real-world applicability. To enable practical use of OECT-based biosignal monitoring devices, efforts must prioritize both long-term reliability and high performance. This requires accurate, sustained signal monitoring alongside electrical and mechanical stability, extended shelf-life, and sterilization resilience to ensure consistent and secure skin attachment. Three key factors must be addressed for effective long-term biosignal monitoring: i) low power consumption with high-amplification across varying signal polarities, ii) robust stability during operation, storage, and sterilization, and iii) mechanical softness for reliable adhesion to the complex skin surface upon dynamic mechanical stimuli. Addressing these challenges during the device development phase is essential for the successful application of OECTs as reliable and durable biosignal recorders.

State-of-the-art organic electrochemical transistors (OECTs) for biosignal recording have gained attention by utilizing depletion-mode PEDOT:PSS, which enables peak transconductance (g_m) to be achieved

* Corresponding authors.
** Corresponding author at: Department of Intelligence Semiconductor, Ajou University, Suwon 16499, Republic of Korea.
E-mail addresses: keehoon.kang@snu.ac.kr (K. Kang), jgmei@purdue.edu (J. Mei), sj0223park@ajou.ac.kr (S. Park).
[1] These authors contributed equally to this work.
[2] Present address: Cavendish Laboratory, University of Cambridge, Cambridge, CB3 0HE, UK

https://doi.org/10.1016/j.mser.2025.101003
Received 27 December 2024; Received in revised form 10 March 2025; Accepted 21 April 2025
Available online 6 May 2025

near zero gate voltage (V_G), thus reducing the continuous power consumption typically required in accumulation-mode OECTs [4,5]. Despite achieving high transconductance values exceeding 400 mS [3], a significant limitation of depletion-mode PEDOT:PSS is its imbalance in transduction capability, restricting effective biosignal transduction to the negative potential range. While PEDOT:PSS reduces power consumption, signal amplification in the positive potential range is notably diminished due to low transconductance (g_m), which hampers accurate monitoring and diagnosis of biosignals that span both positive and negative potential ranges [6]. To overcome this limitation, there is a growing demand for *n*-type depletion-mode OMIECs in OECT-based biosignal recording devices. Recent advancements have demonstrated high μC^* values exceeding 700 F cm^{-1} V^{-1} s^{-1}, which was record-high material characteristic that facilitates efficient charge transport and ionic coupling, resulting in transconductance values of 6.1 mS, underscoring the potential of *n*-type OMIECs for sensitive and efficient biosignal monitoring applications [7–9].

However, developing biosignal recording devices based on *n*-type materials still remains challenging. The key characteristics essential for their successful application in real-world scenarios such as record-high transconductance, superior stability, and skin-conformal stretchability are difficult to be simultaneously satisfied from a single active material. A primary obstacle in advancing *n*-type depletion-mode OMIECs is the energetic position of their lowest unoccupied molecular orbital (LUMO) levels, which often lie near the oxygen reduction potential. This makes *n*-type materials highly vulnerable to oxidative degradation, severely limiting their long-term operation in ionic aqueous solution [7,10,11]. Additionally, channel materials must endure external environmental stresses, such as UV exposure or autoclaving, which are essential for maintaining device cleanliness and sterility before attachment. Without proper sterilization, bacterial and microbial accumulation may pose significant health risks [5,12–14]. These processes are standard sterilization procedures applied to help remove bacteria and contaminants for devices/gadgets that function in contact with human bodies, but many organic channel materials cannot endure these harsh conditions due to their weak intermolecular bonding, leading to degradation and compromising stability. Furthermore, the dynamic, microstructured, and constantly changing surface of the skin demands materials that can achieve conformal adhesion. Skin motion and deformation can significantly affect the device performance, making it crucial to design materials and devices that maintain reliable adhesion and prevent stress concentration during mechanical deformation, thereby ensuring durability under strain.

In this work, we present an ultraflexible 4-terminal vertical Corbino OECT (4-T vcOECT) featuring an n-doped poly(benzodifurandione) (n-PBDF) film, which is a highly conductive (~4038 S/cm) *n*-type polymer [15,16]. By capitalizing on our 4-T device structure [3], μC^* value was measured to be 1787 F cm^{-1} V^{-1} s^{-1}, yielding a g_m of 374 mS in the vertically structured Corbino device. This configuration achieved cutoff frequencies (f_c) up to 1.2 kHz with negligible on-current variation after 4000 on/off cycles. The device maintained both current and g_m values even after 1000 cycles of repetitive tensile strain testing at a tight bending radius of 5 μm, which is attributed to the isotropic stress distribution accommodating strains of up to 200 %. Additionally, the devices exhibited exceptional shelf-life stability, with g_m values showing negligible changes after 8 h under conditions of 85 % relative humidity, immersion in aqueous electrolyte (0.1 M NaCl), and phosphate-buffered saline (PBS). The devices also endured UV- and autoclave sterilization conditions, showing negligible performance changes. This stability was attributed to the low LUMO level of −4.94 eV. Notably, the 4-T vcOECT successfully recorded electrocardiogram (ECG) signals at an operational voltage of just 10 mV, delivering a signal-to-noise ratio of 38.1 dB over 7 days. This achievement represents a significant step toward the practical application of long-term biosignal monitoring devices using *n*-type OMIECs.

2. Molecular design and material characterization of n-PBDF

The molecular structures of n-PBDF (doped) and PBDF (dedoped) during the electrochemical reactions are illustrated in Fig. 1a. As a depletion mode OMIEC, n-PBDF is initially doped, with its charge carriers counterbalanced by cations [15]. Reversible doping and dedoping processes were achieved by applying a potential to the polymer through a 0.1 M NaCl aqueous solution, as illustrated in Figure S1. In the 0.1 M NaCl aqueous electrolyte, cyclic voltammetry reveals reversible electrochemical redox reactions within a potential range of 0.8 to −0.3 V versus an Ag/AgCl reference electrode. A spectroelectrochemical analysis, conducted with a potential sweep from 0.9 to −0.4 V versus an Ag/AgCl reference electrode, revealed three primary peaks: two neutral peaks at $\lambda \sim 515$ nm and 870 nm, and a polaronic peak at $\lambda > 1200$ nm. The application of a negative potential increased the intensity of the polaronic peak, while the neutral peaks diminished, indicating effective reduction of the n-PBDF film. Conversely, under positive potential, the polaronic peak diminished, and the neutral peaks recovered in the intensity, reflecting the subsequent oxidation of the n-PBDF film. This electrochemical behavior demonstrates the reversible doping and dedoping capabilities of n-PBDF, validating its suitability as an active layer for OECT devices.

To enhance charge and ion transport properties, the n-PBDF polymer was incorporated into a vertical Corbino device structure (Figs. 1b and 1c), forming a film on the planar (region I) and vertical (region II) channel areas (Fig. 1d). The channel length and width were precisely controlled by the thickness of the parylene-C (PaC) layer between the top and bottom metal electrodes and the perimeter of the via hole, respectively. To explore the electrical, electrochemical, and microstructural properties of the films formed on the vertical and planar surfaces, samples were prepared as illustrated in Figure S2. Cyclic voltammetry and spectroelectrochemical analyses revealed comparable behavior across both orientations, indicating no significant differences in their electrochemical characteristics (Figure S3). Consistent conductivity measurements from four-point probe analyses further validated that the n-PBDF film maintained uniform electrical performance before and after doping, regardless of the film formation direction (Figure S4). Surface morphology and roughness, along with the uniformity of current signal distribution within conductive regions, were assessed using atomic force microscopy in conductive probe mode. Despite distinct preparation methods, the films demonstrated nearly identical surface profiles, with root-mean-square roughness values of 1.38 nm for the planar film and 1.72 nm for the vertical film, highlighting their uniformity and high quality (Fig. 1e and Figure S5).

To explore the microstructural differences in planar and vertical n-PBDF films, grazing-incidence wide-angle X-ray scattering (GIWAXS) measurements were performed on n-PBDF films prepared on parylene-C substrates with distinct coating configurations (Figure S6 and Table S1). In the vertical Corbino OECT configuration, the channel region is oriented perpendicular to the substrate, with its surface interfacing with the parylene-C layer, as illustrated in Fig. 1b and d. Therefore, the distinct film preparation method shown in Figure S6 were designed to replicate the conditions under which n-PBDF films form on the vertical parylene-C surface (Region II in Fig. 1d) within our device structure. Both configurations predominantly exhibited an edge-on molecular orientation, characterized by lamellar (100) peaks at $q_z = 0.59$ and 0.58 Å^{-1} (d-spacing = 10.66 and 10.73 Å) and π−π stacking (010) peaks at $q_{xy} = 1.87$ and 1.88 (d-spacing = 3.36 and 3.34 Å) for planar and vertical configurations, respectively. These results confirm that the coating configuration does not influence the microstructure of n-PBDF films on parylene-C. Furthermore, to examine the effects of electrochemical changes, GIWAXS measurements were conducted on doped and dedoped n-PBDF samples prepared on ITO glass substrates. The microstructural analysis revealed that the electrochemically doped n-PBDF films (Figs. 1f and 1g) predominantly exhibited an edge-on molecular orientation, characterized by prominent lamellar (100) peaks at

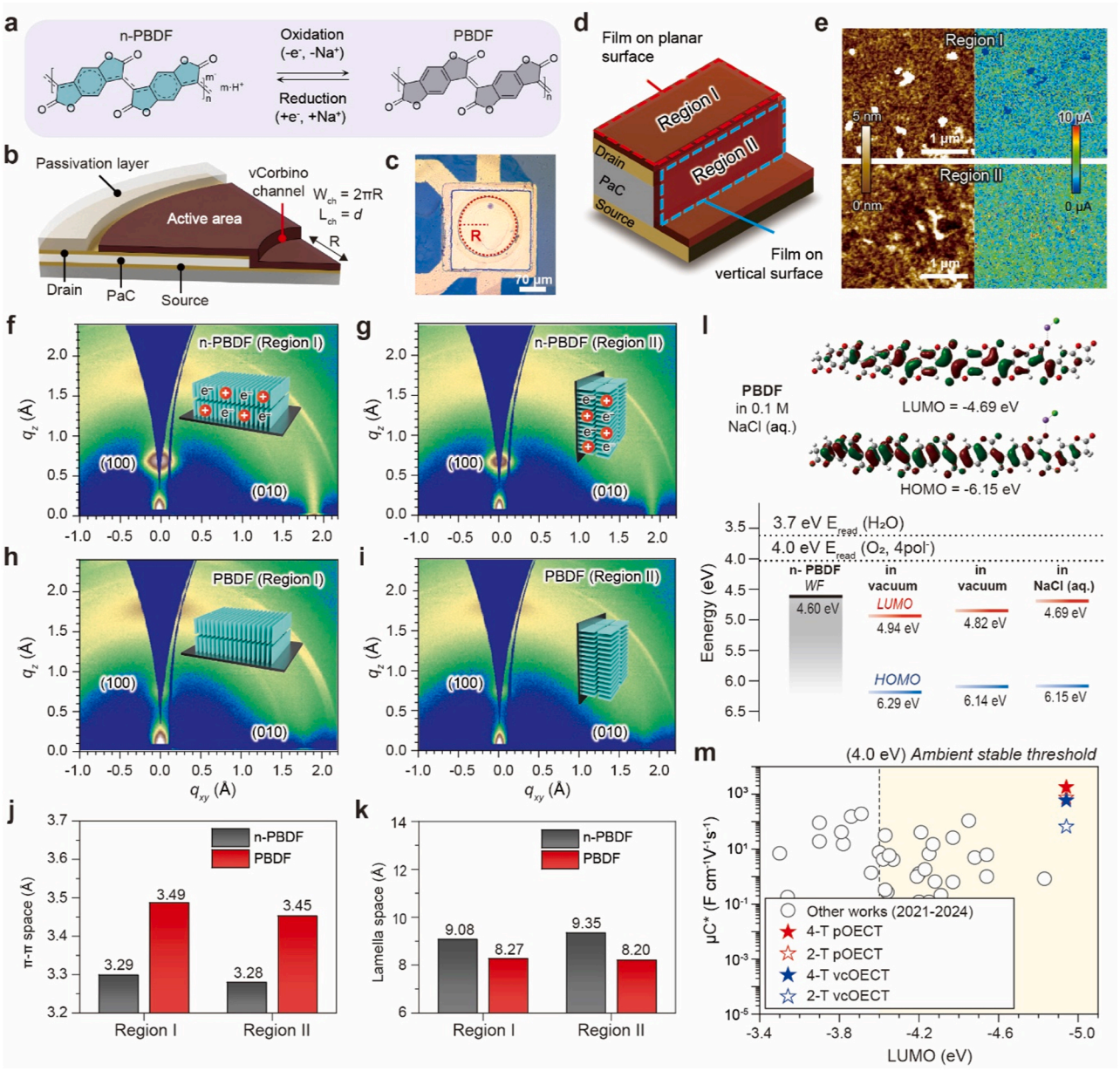

Fig. 1. Design and characterization of n-PBDF-based vertical Corbino organic electrochemical transistors (vcOECT) a, Molecular structure of n-doped PBDF (n-PBDF) and PBDF under electrochemical reactions. **b,** Schematic of vcOECT device structure using n-PBDF. **c,** Optical microscope image of vcOECT device (scale bar: 50 μm). **d,** Schematic representation of channel region of vcOECT device. Region I represents the n-PBDF film coated on the planar surface, while region II represents the n-PBDF film coated on the vertical surface. **e,** Atomic force microscopy (AFM) height and conductive AFM (c-AFM) images. 2D-grazing-incidence wide-angle X-ray scattering (GIWAXS) pattern of (**f, h**) planar and (**g, i**) vertical configurations of n-PBDF films after electrochemical doping (**f, g**) and dedoping (**h, i**) in 0.1 M NaCl aqueous electrolyte (−0.3 V and 1.0 V vs. Ag/AgCl reference electrode). (inset: schematic of the polymer orientation for each condition and film configuration). **j,** π−π, and **k,** lamellar stacking distances extracted from in-plane and out-of-plane line-cut profiles of n-PBDF and PBDF films in the two film configurations, subjected to electrochemical doping and dedoping. **l,** Energy level distributions of PBDF film from density functional theory calculations: vacuum, water, and 0.1 M NaCl aqueous electrolyte and work function of n-PBDF. **m,** Plot of μC^* and LUMO level of *n*-type OMIECs reported in the literature from 2021 to 2024.

$q_z = 0.69$ and 0.67 Å^{-1} (*d*-spacing = 9.08 and 9.35 Å) and π−π stacking (010) peaks at $q_{xy} = 1.91$ and 1.92 Å^{-1} (*d*-spacing = 3.29 and 3.28 Å). Upon dedoping, the films maintained an edge-on orientation, with lamellar (100) peaks shifting to $q_z = 0.76$ and 0.77 Å^{-1} (*d*-spacing = 8.27 and 8.20 Å) and π−π stacking (010) peaks shifting to $q_{xy} = 1.80$ and 1.82 Å^{-1} (*d*-spacing = 3.49 and 3.45 Å) (Figs. 1h and 1i). A quantitative comparison of these structural parameters (Figs. 1j and 1k, Figure S7, and Table S2) revealed that the changes in π−π and lamellar stacking distance during doping/dedoping were similar for planar and vertical films. These all findings demonstrate that the film preparation method did not affect the electrochemical, electrical, morphological, or structural properties of the films.

All the *d*-spacing values obtained from GIWAXS are consistent with those previously reported for PBFDO [7–9], which shares the same molecular structure. This similarity indicates that n-PBDF is expected to exhibit superior charge transport characteristics. Indeed, as shown in Table S2, the crystallographic parameters of n-PBDF, including coherence length, π−π stacking distance, and lamellar spacing, are indicative of high-performance charge transport properties [17,18]. Moreover, the robust structural ordering of n-PBDF, which remains intact even after

doping, is recognized as a critical factor that enhances its charge mobility [19]. This structural robustness is one of the key elements expected to contribute to its superior charge transport properties, highlighting the molecular structure of n-PBDF as an excellent design for efficient *n*-type mixed ionic−electronic transport. In particular, the molecular orientation of the n-PBDF film remained unchanged in the vertical channel area (region II), suggesting that the vertical device configuration benefitted from the edge-on molecular orientation, advantageous for both charge and ion transport in the vertical device structure [20,21]. These results emphasize the critical role of molecular

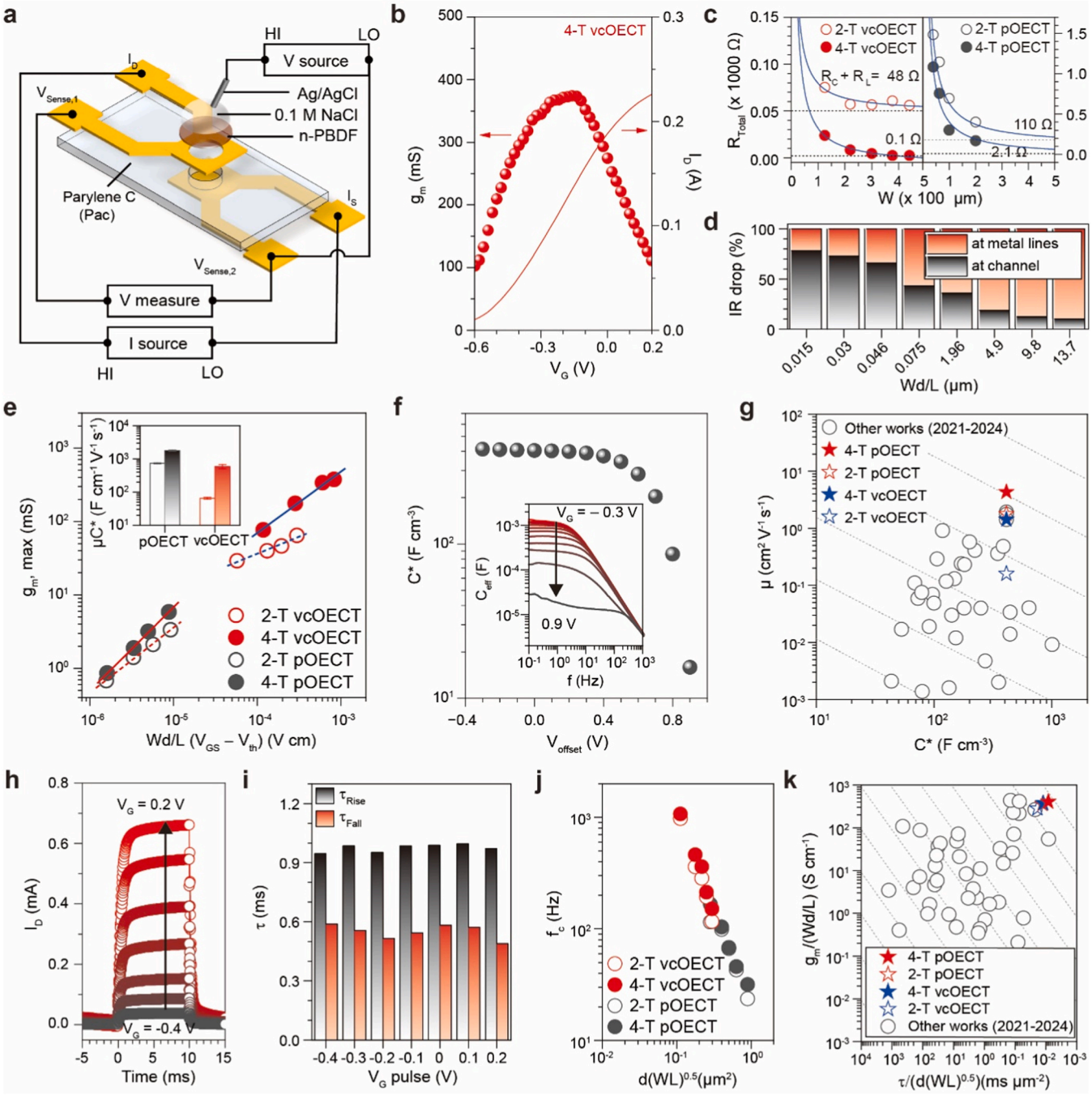

Fig. 2. Electrical characterization of OECT devices. a, Schematic representation of the 4-T vcOECT device and measurement configuration. **b,** Transfer curve and g_m values of 4-T vcOECT. **c,** Comparison of total resistance between 2-T and 4-T OECT according to the channel width. **d,** Relative *IR* drop at channel and metal line as a function of *Wd/L*. **e,** g_m values as a function of $Wd/L(V_{GS}-V_{Th})$, obtained from vcOECT (red circle) and pOECT (black circle). The filled and empty symbols indicate those measured by the 4-T and 2-T measurement configurations, respectively. Inset shows μC^* values extracted from each measurement condition. **f,** Volumetric capacitance of n-PBDF film obtained by electrochemical impedance spectroscopy (EIS) as a function of V_{offset}. All values were extracted from the capacitance value at 1 Hz of sinusoidal V_{offset} signal. Inset shows the effective capacitance obtained from the EIS measurements of the n-PBDF film on the ITO electrode. Line color denotes V_{offset} from −0.3 to 0.9 V (red to black). **g,** $\mu-C^*$ map of previously reported *n*-type OMIECs. The dotted lines denote the constant μC^* product. **h,** Transient response of the drain current at a constant V_D of 0.01 V and a square voltage pulse of 10 ms (V_G=0.1–0.7 V) at the gate electrode. **i,** Plot of rise and fall time constants obtained from the transient response (from Fig. 2h). **j,** Plot of cut-off frequency value as a function of channel geometry factors relevant to the time constant values. **k,** Benchmarking of previously reported *n*-type OMIECs and n-PBDF herein by comparing their corresponding steady- and transient-state performances. For a fair comparison, the transconductance was normalized by (*Wd/L*), and the time constant was normalized by $d(WL)^{0.5}$.

orientation in determining charge and ion transport properties in vertical OECT configurations.

For *n*-type OMIECs, stability in both air and aqueous environments is of paramount importance. It is noteworthy that PBDF exhibits excellent stability under ambient conditions, which can be attributed to its deep lowest unoccupied molecular orbital (LUMO) level of −5.1 eV and a work function of −4.6 eV for n-PBDF [15]. To further evaluate its performance in aqueous electrolyte-based OECTs, the energy levels of PBDF were calculated in various environments, including vacuum, water, and an aqueous electrolyte (0.1 M NaCl (aq.)), using density functional theory (DFT) (Fig. 1l and Figure S8). The calculations revealed minimal variation in the highest occupied molecular orbital (HOMO) levels, but a stepwise shift in the LUMO level was observed, resulting in a deeper LUMO energy level of −4.69 eV. This finding highlights the remarkable stability under both aqueous and ambient conditions [22,23], a key attribute for advancing n-type conjugated (semi-)conducting polymers.

These materials are being actively developed with deeper LUMO levels to enhance device performance and durability. Density Functional Theory (DFT) calculations of PBDF and n-PBDF torsion angles reveal that the PBDF backbone adopts a distorted conformation to stabilize Coulombic repulsion between adjacent monomer units (Figure S9) [24,25]. This slight increase in dihedral angle, which stabilizes the molecular structure, results in tighter π−π stacking and enhanced coherence lengths within the crystallized domains upon doping (Table S2) [26]. Such structural refinements are instrumental in supporting the superior charge transport properties of n-PBDF. Together with its robust electrochemical properties and exceptional electrical performance, n-PBDF emerges as a compelling candidate for long-term application in stable, high-performance electrochemical devices (Fig. 1m).

3. Electrical characterization of n-PBDF OECT

We determined the electrical properties of n-PBDF by using a 4-T vertical Corbino organic electrochemical transistor (vcOECT) configuration, as shown in Fig. 2a and Figure S10. In the 4-T configuration, a current was applied between the source (I_S) and drain (I_D), while the voltage drop between the source and drain was measured using a voltmeter connected to $V_{Sense,1}$ and $V_{Sense,2}$. Gate voltage (V_G) was applied to the n-PBDF through a 0.1 M NaCl electrolyte in direct contact with an Ag/AgCl non-polarizable electrode. This configuration ensures that only the *IR* drop associated with the contact resistance (R_C) and channel resistance (R_{Ch}) is considered, while the line resistance (R_L) is effectively excluded (Figure S11). In a standard 2-terminal measurement configuration, the applied drain voltage (V_D) and measured drain current result in a voltage drop across the entire series resistance, including R_L, R_C, and R_{Ch}. However, in the 4-T measurement configuration, two terminals (I_S and I_D) are dedicated to supplying current, while the other two ($V_{Sense,1}$ and $V_{Sense,2}$) are used solely for voltage measurement. Since no voltage source is directly applied in this 4-T setup, the current supplied is adjusted to ensure that the voltage measured between $V_{Sense,1}$ and $V_{Sense,2}$ equals the set V_D. Due to the high internal impedance of the voltmeter, it exclusively measures the voltage drop across R_C and R_{Ch}, effectively eliminating the influence of R_L. As a result, V_D is accurately applied only to the R_C and R_{Ch}, significantly enhancing the effective voltage applied to the channel. This reduction in parasitic resistance leads to a higher transconductance in the 4-T configuration compared to the 2-T configuration, regardless of the device structure. This is achieved by utilizing the same number of source-measure units while employing the 'four-wire sense mode' (see Device characterization section), as we demonstrated previouesly [3].

As shown in Fig. 2b and S12, the 4-T measurement configuration yields higher transconductance (g_m) and I_D values compared to the 2-T configuration, irrespective of whether the channel is in a vcOECT or planar OECT (pOECT) geometry. The 4-T vcOECT exhibited a maximum g_m value of approximately 374 mS, representing one of the highest g_m reported among *n*-type OECTs to date. The V_G required to achieve the maximum g_m value is −0.16 V for the 4-T vcOECT and −0.24 V for the 4-T pOECT, both of which are lower than the V_G values typically reported for accumulation-mode *n*-type OECT devices [27–31]. Furthermore, at $V_G = 0$ V and $V_D = 0.4$ V, the g_m values were 275 mS and 4 mS for the 4-T vcOECT and pOECT, respectively, highlighting the potential for low power consumption, rendering it particularly suitable for efficient biosignal sensing, especially in the positive signal range.

To evaluate the influence of the voltage drop over the line resistance, R_L on the total resistance of the device, R_{Total} ($R_{Total} = R_{Ch} + R_C + R_L$ where R_{Ch} is the channel resistance and R_C is the contact resistance) values were extracted from the plot of R_{Total} as a function of the channel width, *W* (Fig. 2c). The results show the extracted $R_C + R_L$ values significantly drop from 48 Ω to 0.1 Ω for vcOECT and from 110 Ω to 2.1 Ω for pOECTs when comparing between the 2-T to 4-T measurement configurations, which demonstrates the effective reduction in the R_L in the 4-T configuration. Furthermore, the R_L values measured in the pOECT were found to be higher than those in the vcOECTs, which can be attributed to the longer length and narrower width of the line electrode geometry as can be seen in Figure S13 (Supporting Information). By considering a potential divider circuit, the relative potential drop ratio, (i.e. *IR* drop ratio), calculated as R_L/R_{Total}, was plotted as a function of the channel geometry parameter *Wd/L*, where *W*, *d*, and *L* represent the channel width, thickness, and length, respectively (Fig. 2d). The relative *IR* drop at R_L varied from 22 % to 90 %, as *Wd/L* increased from 0.015 μm to 13.7 μm, indicating that devices with larger *Wd/L* are more significantly affected by R_L. This behavior is attributed to the proportional reduction of R_{Ch} with increasing *Wd/L*, leading to the larger ratio of $R_L/(R_{Ch} + R_C + R_L)$, and consequently a more pronounced *IR* drop at R_L.

We are now in the position to discuss the figure of merit, μC^* and g_m to evaluate the relative device performance of n-PBDF OECTs by 4-T configuration. The reduction of R_L in vcOECT and pOECT both in the 4-T configuration results in higher value of g_m as shown in Fig. 2e. The slope of the plot in Fig. 2e represents the material's figure of merit, μC^* , as defined by the equation describing the g_m value of the OECT devices [32].

$$g_m = \mu C^* \frac{Wd}{L}(V_G - V_{Th}) \quad (1)$$

where μ is the electronic carrier mobility, C^* is the volumetric capacitance, and V_{Th} is the threshold voltage. From the 4-T measurement configuration, μC^* values of 1787 ± 46 F cm^{-1} V^{-1} s^{-1} for pOECTs and 588 ± 84 F cm^{-1} V^{-1} s^{-1} for vcOECTs were obtained. In comparison, the μC^* values from the 2-T measurement configuration were significantly lower at 736 ± 27 F cm^{-1} V^{-1} s^{-1} for pOECTs and 65 ± 4 F cm^{-1} V^{-1} s^{-1} for vcOECTs (inset of Fig. 2e). Although the vcOECT yields a lower device performance metrics than the pOECT even for 4-T measurement configuration, for applications prioritizing high g_m values, such as in bioelectronics, the 4-T vcOECT configuration remains advantageous (as demonstrated later). In addition, the results highlight that the elimination of the parasitic resistance can drastically enhance the g_m for vcOECTs, highlighting the role of the line resistance for OECT device architectures with short-channels (Figure S14).

To elucidate the high μC^* values of n-PBDF, we first present the electrochemical impedance spectroscopy (EIS) analysis for quantitatively determining the ionic−electronic coupling of n-PBDF, as outlined in the experimental setup in the Supporting Information (Figure S15). From the Bode plots obtained under varying V_{Offset} conditions, effective capacitance (C_{eff}) was calculated (inset of Fig. 2f). The volumetric capacitance (C^*) was determined by normalizing C_{eff} with the volume of n-PBDF film used in the experiment (Figure S15) and plotted as a function of V_{Offset} in Fig. 2f. The results show that the highest C^* value, approximately 400 F cm^{-3}, was achieved in the doped state. As the V_{Offset}, shifted positively, the C^* value decreased, reaching approximately 20 F cm^{-3} in the dedoped state. This behavior clearly indicates

the dedoping process of the n-PBDF film with a positive V_{Offset}, consistent with the classification as an *n*-type depletion mode OMIEC. The C^* value in the doped state is comparable to the previously reported values for n-PBDF [9,15] and is notably high among *n*-type OMIECs.

The C^* values obtained from the EIS measurements allow us to indirectly determine the electron mobility (μ) of n-PBDF in the doped state. As shown in Fig. 2g, the μ values derived using the 4-T measurement configuration were approximately 4.3 $cm^2\ V^{-1}\ s^{-1}$ for pOECT and 1.4 $cm^2\ V^{-1}\ s^{-1}$ for vcOECT (for the highest value of the measured $C^* = 400\ F\ cm^{-3}$), whereas those of the 2-T configuration were 1.8 $cm^2\ V^{-1}\ s^{-1}$ and 0.2 $cm^2\ V^{-1}\ s^{-1}$ for pOECT, and vcOECT, respectively. This represents that the 2-T configuration can underestimate the mobility due to the inclusion of R_L in the circuit. In addition, our result can be understood in light of the high μC^* reported by Huang et al. [8] for PBFDO that shares the identical molecular structure. PBFDO exhibited a remarkable μC^* of 796 $F\ cm^{-1}\ V^{-1}\ s^{-1}$, significantly outperforming previous benchmarks, such as f-BSel2g-SVSCN, which achieved only 191 $F\ cm^{-1}\ V^{-1}\ s^{-1}$ [31] (Table S3). In terms of μ, the best value before PBFDO was 1.1 $cm^{-2}\ V^{-1}\ s^{-1}$, recorded for TIG-T, nearly half that of PBFDO. In this work, we achieved a state-of-the-art μC^* of 1786 $F\ cm^{-1}\ V^{-1}\ s^{-1}$, and a μ of 4.3 $cm^2\ V^{-1}\ s^{-1}$ by employing the 4-T measurement configuration.

The high μ value determined for n-PBDF above can be attributed to the high crystallinity and coherence length (Table S2) of n-PBDF. As discussed previously, n-PBDF films processed in both planar and vertical configurations show densely packed molecular arrangements and high crystallinity (as represented by the relatively high L_c of 60 nm), both of which are well-established as key requirements for enhancing charge transport in OMIECs [17,18]. Furthermore, the stable structural ordering of n-PBDF, even after doping, is considered a key factor driving its high charge mobility [19]. Interestingly, the higher μ value of n-PBDF compared to previously reported PBFDO [7–9], which shares an identical molecular structure, can also be attributed to the enhanced crystallinity. To visualize the excellent material figure of merit relative to other state-of-the-art results reported in previous literature (from 2021 to 2024), Fig. 2g and Table S3 simultaneously plot the μ and C^* values of various *n*-type OMIECs. These comparisons reveal that n-PBDF achieved one of the highest μ values reported to date, even when measured using the 2-T vcOECT configuration.

The transient response of OECT devices is also a crucial figure of merit for the efficient and accurate monitoring of biosignals due to their diverse frequency ranges [33]. The transient responses were evaluated using the measurement setup shown in Figure S16. The vcOECT devices demonstrated a rapid response upon the application of a V_G pulse across varying V_G values (Fig. 2h). The rise and fall times of the device were measured to be within 1 ms and 0.6 ms, respectively (Fig. 2i), irrespective of the V_G value. These measurements were conducted using a device with a channel radius of 10 μm ($W = 62.8$ μm).

The frequency response provides insight into the range of signals that the device can handle without a significant loss of g_m. The measurement setup for the frequency response and the results for various device geometries are shown in Figure S17. The cut-off frequency (f_c), defined as the frequency at which the g_m value decreased by 3 dB from its initial value (dashed line in Figure S17), was obtained and plotted in Fig. 2j. For vcOECTs, f_c values ranged from 166 Hz to 1072 Hz for channel widths ranging from 440 μm to 63 μm. Notably, the devices measured using the 4-T configuration exhibited slightly faster response times, indicating that the reduction in R_L influences the response time of the device. This improvement is likely due to changes in the resistance component in the ionic circuit, which directly affect the *RC* time constant. This linear trend of f_c value as a function of $d(WL)^{0.5}$ aligns well with theoretical predictions based on the *RC* time constant [34].

Overall, we can systematically compare the performance of our device with other previously reported *n*-type OECT devices of various channel dimensions by normalizing both the transconductance and response time to the geometrical factor (Wd/L), as shown in Fig. 2k. This plot offers valuable insights into evaluating the potential of the devices for biosensing applications that demand both high sensitivity (i.e., a high transconductance) and 2) rapid responsiveness to biosignals (i.e., a fast response time). The results demonstrate that our devices achieve the highest performance metrics in both transconductance and response time. This exceptional performance can be attributed to the 4-T vertical Corbino device platform, which eliminates parasitic resistance in the circuit, effectively leveraging the intrinsically superior mixed-conduction properties of n-PBDF. This approach is particularly advantageous for vertical devices, where parasitic resistance tends to have a more pronounced impact.

4. Device operational stability and sterilization resilience of n-PBDF OECTs

Shelf-life stability poses a significant challenge for *n*-type semiconductors due to their susceptibility to degradation in ambient conditions [22]. To assess the stability of the n-PBDF OECTs, humidity tolerance tests were conducted in a chamber with relative humidity (RH) levels incrementally adjusted from 0 % to 100 % in 20 % steps. Transfer curves were measured at each RH condition and displayed as contour plots (Fig. 3a-d). PEDOT:PSS OECTs were used as reference devices for comparison.

The results showed that the PEDOT:PSS OECTs experienced notable performance degradation, with peak g_m values decreasing by 31 % (from 3.2 to 2.2 mS) in planar devices and by 16 % (from 34.9 to 29.1 mS) in vertical devices (Figure S18). In contrast, the n-PBDF OECTs demonstrated superior stability, with peak g_m values showing only minor decreases of 8 % (from 2.4 to 2.2 mS) for planar devices and 4 % (from 40.8 to 39.0 mS) for vertical devices. Long-term shelf-life tests further confirmed the stability of the n-PBDF OECTs. The devices were stored under harsh conditions, including RH 85 %, immersion in 0.1 M NaCl aqueous solution, and PBS solution, and their performance was monitored over time (Fig. 3e-g). After up to 8 h of storage under these conditions, the n-PBDF OECTs exhibited minimal g_m losses of 1–3 %. By comparison, PEDOT:PSS OECTs showed significantly higher g_m losses of 10–24 % under identical storage conditions. These results establish n-PBDF as a robust material for reliable, long-term operation in OECT-based biosignal monitoring devices.

To evaluate the long-term operational stability of the n-PBDF OECTs, repetitive on/off cycling tests were performed. The results, shown in Fig. 3h, demonstrate reliable device operation, with only a 0.89 % drain current loss observed after 4000 on/off cycles with V_D of 10 mV. This corresponds to continuous operation for over an hour in the PBS solution. We also compared the operational stability of our device with other OECTs reported in Table S4. While a direct comparison is challenging due to variations in test conditions, making the analysis inherently qualitative, our findings suggest that the operational stability of n-PBDF stands out among OMIECs with a μC^* value exceedingly approximately 100 $F\ cm^{-1}\ V^{-1}\ s^{-1}$. Intriguingly, the drain current loss increased significantly to 49 % when the operational V_D was raised to 500 mV, indicating that higher operational voltages not only increased power consumption but also negatively impacted the device stability. This emphasizes the advantage of the low-voltage operation of our 4-T vcOECT configuration, demonstrating practical benefits in power consumption while maintaining operation stability without compromising performance, which are crucial factors for long-term bioelectronic devices intended for clinical applications.

For practical biomedical applications, devices must endure sterilization processes to prevent contamination and inflammation. To assess this, we tested the device performance after UV and autoclave sterilization. Devices were exposed to UV light at wavelengths of 365 nm (610 $\mu W\ cm^{-2}$) and 256 nm (400 $\mu W\ cm^{-2}$) for up to 30 minutes, corresponding to a cumulative UV energy dose of approximately 1.1 $J\ cm^{-2}$. Even under these conditions, which far exceed the typical sterilization dose of 20 $mJ\ cm^{-2}$ required to eliminate 99.9 % of germs [35], the

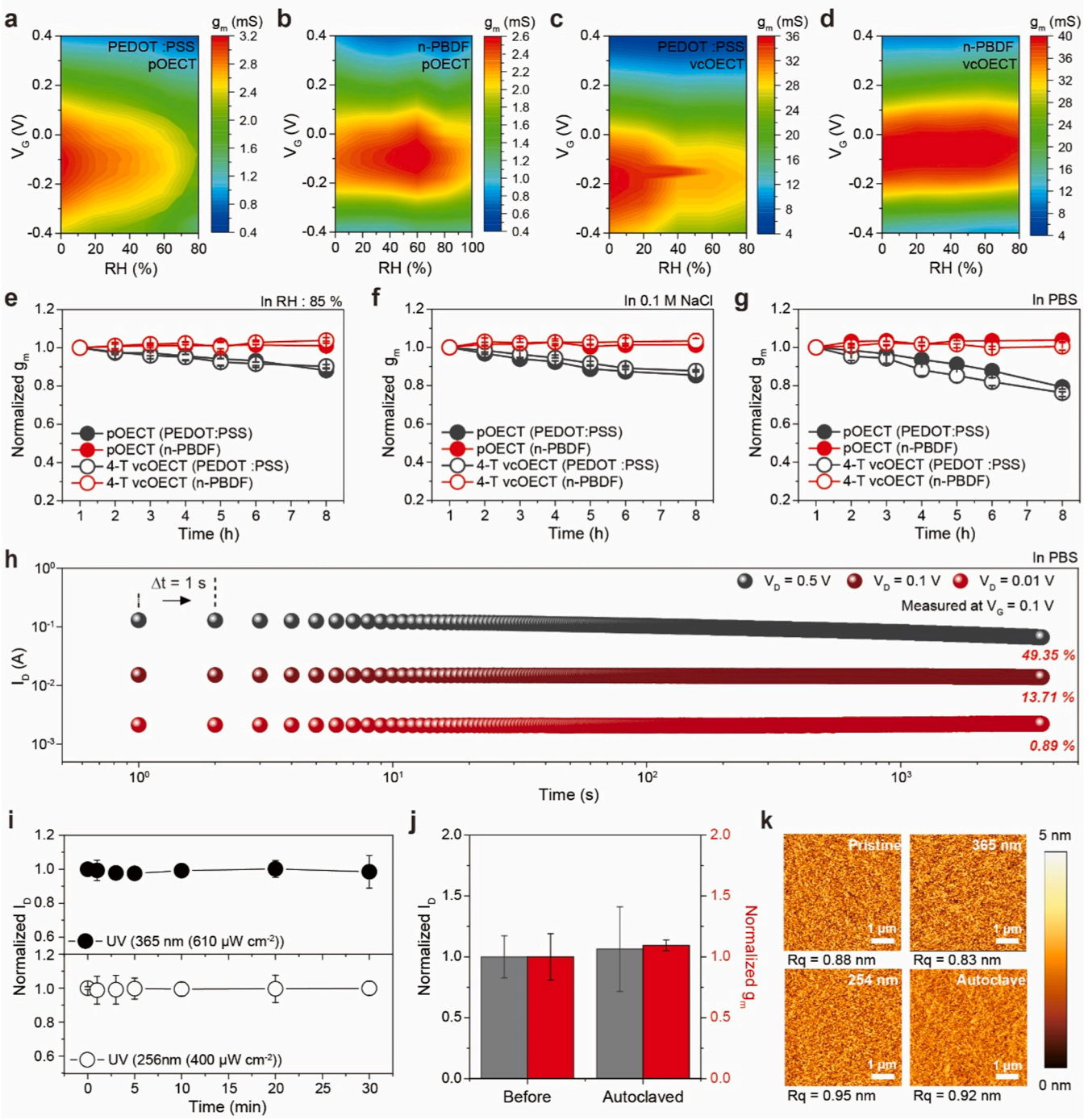

Fig. 3. Highly stable OECT characteristics. The color-coded contour plots of transconductance of **a,** PEDOT:PSS 4-T pOECT; **b,** PEDOT:PSS 4-T vcOECT; **c,** n-PBDF 4-T pOECT; **d,** n-PBDF 4-T vcOECT. Comparison of normalized transconductance of **e,** in relative humidity of 85 %, **f,** in 0.1 M NaCl aqueous solution, and **g,** in PBS solution. Black circles represent PEDOT:PSS 4-T OECTs and red circles represent n-PBDF 4-T OECT, with filled and empty symbols indicating pOECT and vcOECT, respectively. **h,** Cycling stability of 4-T vcOECT where V_D = 0.01 V, 0.1 V, and 0.5 V. V_G is switching between 0.1 V and 0.1 V (R=140 μm, W= 439.6 μm, L=500 nm). **i,** UV sterilization test of n-PBDF OECT devices with different UV wavelengths and sterilization times. **j.** Comparison of on-current and maximum transconductance values of OECT devices before and after different sterilization processes. **k,** AFM images and surface roughness values of n-PBDF films before and after sterilization processes.

devices retained their performance with no significant loss in peak g_m values (Fig. 3i, Figure S19). The devices also maintained their performance following autoclave sterilization, showing minimal loss in the peak g_m values (Fig. 3j and Figure S20). The surface morphologies of the n-PBDF films before and after sterilization were examined using AFM (Fig. 3k). Although a slight increase in R_q was observed, the overall film morphology remained intact, indicating negligible changes in the mixed conduction properties of the n-PBDF films.

5. Skin-conformal epidermal signal monitoring sensor with mechanical reliability

To enable a skin-conformal electrocardiogram (ECG) monitoring sensor, the devices must demonstrate reliable performance under strain-

induced deformations, replicating real-world on-skin operational environments. This requires high flexibility and the ability to stretch by up to 30 % strain, accommodating body movements while maintaining the sensing capabilities [36,37]. To evaluate mechanical stability, we fabricated 3-micrometer-thick ultraflexible vcOECTs with n-PBDF channels (Figure S21). These delaminated flexible n-PBDF vcOECTs were carefully transferred onto a pre-stretched polymeric elastomer. The elastomer stretched to 200 % of its original length (200 % tensile strain) and gradually relaxed back to 0 % tensile strain (Fig. 4a). The ultraflexible n-PBDF vcOECT exhibited negligible changes in the transfer curves and g_m plots across tensile strains ranging from 0 % to 200 % in 50 % increments. This stability is attributed to the vertical channel design, which ensures that the current path remains unaffected by in-plane mechanical deformation. Additionally, the circular geometry of the device facilitates even stress distribution, thereby minimizing the localized strain. Repeated mechanical deformation tests further highlighted the durability of the device. After 1000 cycles of mechanical strain, the maximum I_D decreased marginally from 3.3 to 2.9 mA, while the maximum g_m reduced only slightly from 6.3 to 5.9 mS demonstrating excellent mechanical reliability (Fig. 4d and Figure S22).

The ultraflexible n-PBDF vcOECT demonstrated skin-conformability and functionality as an ECG monitoring sensor. With a thickness of just 3 μm, the device adhered seamlessly to the skin, minimizing gaps and ensuring a robust interface. This conformal contact reduces the skin-

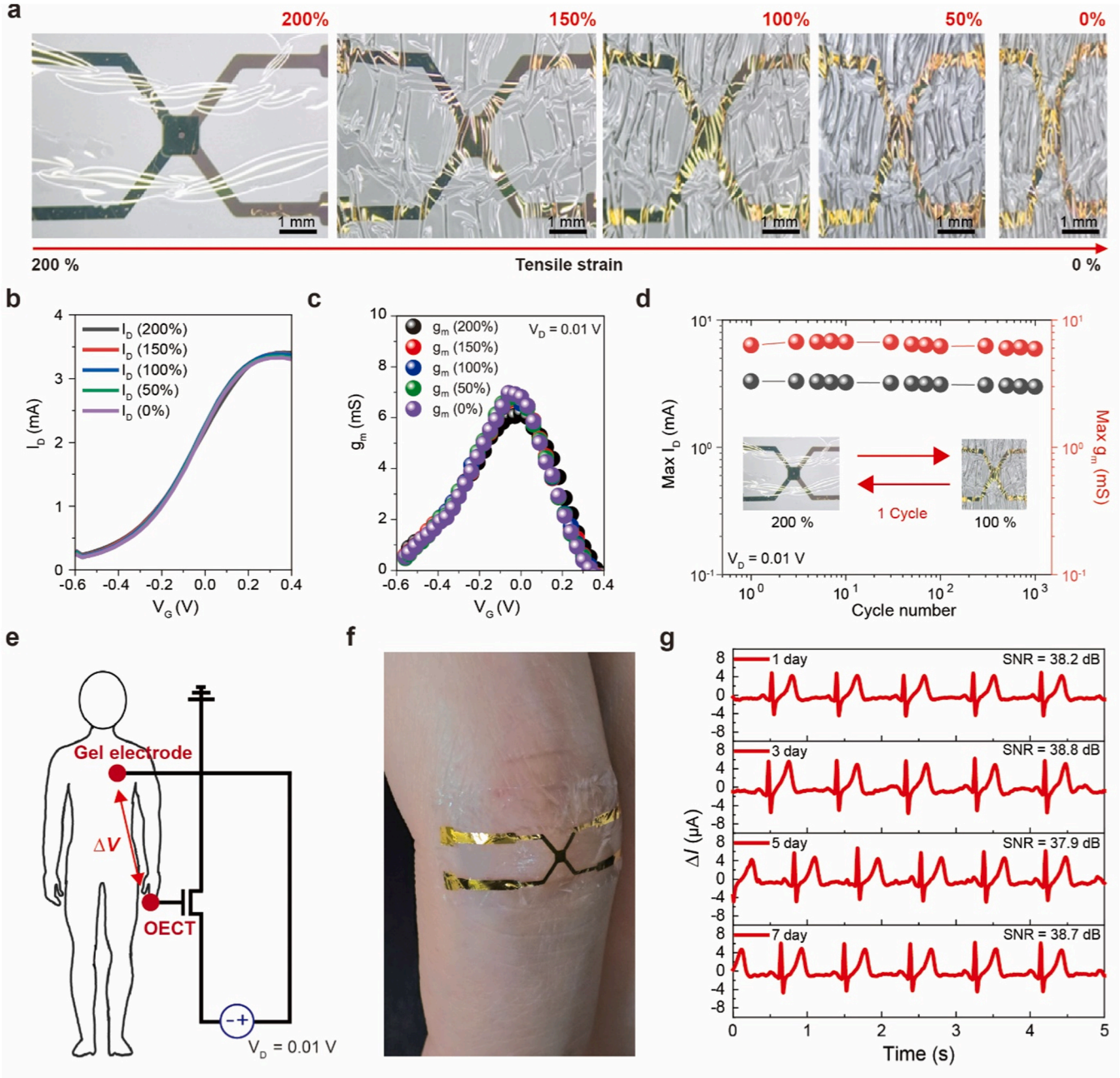

Fig. 4. Operational reliability under mechanical deformation and physiological monitoring via skin-compatible 4-T vcOECT. a, Photograph with tensile strain ranging from 200 % to 0 %. **b-c,** Transfer curve and transconductance characteristics at various mechanical deformations of tensile strain ranging from 200 % to 0 %. **d,** maximum drain current and transconductance values of ultraflexible 4-T vcOECT under repetitive cycles of compression−release (between 100 % and 200 %) with V_D= 0.01 V. **e,** Circuit diagram and measurement setup of ECG recording using flexible 4-T vcOECTs. **f,** Photograph of the flexible 4-T vcOECTs attached to a finger. **g,** ECG signals recorded over one week from the index finger using an ultra-flexible 4-T vcOECT (channel radius (R) of 70 μm, channel width of 439.6 μm, channel length (L) of 500 nm, and V_D= 0.01 V).

interface impedance, enabling a higher signal-to-noise ratio (SNR) for accurate biosignal monitoring. The channel of the ultraflexible n-PBDF OECT was attached to a fingertip using a drop of PBS solution, facilitating capillary action for secure adhesion. A gel electrode attached to the chest served as the ground (source electrode). The potential difference between the chest gel electrode and OECT channel modulated the channel conductivity, allowing real-time cardiogram signals to be recorded as changes in I_D.

The device adhered reliably to the wrinkled fingertip surface (Fig. 4f) and maintained stable performance even during joint movement. This was confirmed by impedance measurements at the device-skin interface (Figure S23), which showed negligible impedance variation before and after finger flexion and extension for the flexible substrate-based device. In contrast, the rigid substrate exhibited noticeable changes, likely due to reduced skin conformity and increased mechanical discontinuities. ECG signals were recorded for 5 seconds every two days over a 7-day period. After each measurement, the device was carefully removed, stored under controlled conditions, and reattached for subsequent measurements. These recordings showed a consistent high SNR of 38.1 dB, even after prolonged exposure to the PBS solution. This high SNR is attributed to the skin-conformability of the ultraflexible n-PBDF vcOECT and the 4-T measurement configuration, which minimizes impedance caused by the gap between the skin and device, as well as parasitic resistance. All measurements were conducted under low operational voltage conditions ($V_D = -10$ mV and $V_G = 0$ V), confirming the low power consumption of the device.

6. Conclusion

Our research demonstrates skin-conformal biosignal monitoring devices, utilizing *n*-type organic mixed ionic−electronic conductor (OMIEC) n-PBDF as the channel material. Structural analysis revealed that n-PBDF exhibited high crystallinity and a deep-lying LUMO, which are attributed to significantly enhance its mixed conduction properties and material stability. By incorporating a 4-terminal (4-T) measurement configuration, we effectively minimized parasitic resistance, achieving a state-of-the-art transconductance value approaching 400 mS. Comprehensive stability testing, including shelf-life, operational stability, sterilization resilience, and mechanical robustness, demonstrated that our device meets or exceeds the requirements of real-world applications. Using ultraflexible substrates seamlessly integrated with 4-T vcOECT devices, the system successfully captured electrocardiogram signals over extended monitoring periods, maintaining an outstanding signal-to-noise ratio. As the demand for non-invasive health monitoring platforms continues to grow, our findings pave the way for the development of more robust, efficient, and sophisticated bioelectronic devices for clinical integration.

7. Materials and methods

7.1. Materials

The n-PBDF conducting polymer, n-doped poly(benzodifurandione) was synthesized as reported in a previous study.[15] All the reagents and solvents for the synthesis and analysis were purchased from Sigma-Aldrich, Alfa Aesar, and TCI and were used without further purification.

7.2. Film characterizations

Atomic force microscopy (AFM) and conductive AFM: Surface morphology and current topography of the prepared thin films were analyzed using an atomic force microscope (AFM) (NX10, Park Systems) equipped with the conductive mode. Conductive diamond-coated silicon probes were used, with current mapping measured while grounding the sample edges using silver paste.

Electrochemical and spectroelectrochemical measurements: All electrochemical measurements were performed in a cell with a leakless Ag/AgCl reference electrode (eDAQ Inc.) and a platinum wire (0.5 mm diameter) as the counter electrode, in a 0.1 M NaCl aqueous electrolyte. The films were preconditioned via cyclic voltammetry (CV) for at least three cycles to achieve stable readings before data collection. Spectroelectrochemical data for the thin films were obtained using an Agilent Cary 5000 UV–vis spectrometer connected to an SP-150 Potentiostat (Biologic Inc.) in a quartz cuvette. Ferrocene/ferrocenium (Fc/Fc^+) served as the external standard for the reference electrode.

Grazing-incidence wide-angle X-ray scattering (GIWAXS): GIWAXS measurements were conducted at the 11-BM CMS beamline at NSLS-II in a vacuum environment using Pilatus 900k detector and a photon energy of 13.5 keV. The sample detector distance was nominally 260 m, and the angle of incidence varied between 0.1 and 0.14 degrees relative to the substrate. Analysis was performed using the Nika software package for wavemetrics Igor Pro.[38]

Density functional theory (DFT) calculations: All DFT calculations were performed using the Gaussian 16 software package [30]. The copolymer structure of PBDF, in both neutral and doped states, was optimized at the B3LYP/6–311 +g(d,p) and UB3LYP/6–311 +G(d,p) [39–41] levels of theory for the solvent system using the IEFPCM[42] solvent model. The optimized structure was also confirmed by frequency analysis and included the zero-point vibrational energy.

7.3. Ultraflexible OECT fabrication

To fabricate ultraflexible substrates, the glass substrates were sequentially cleaned with deionized water, acetone, and isopropyl alcohol for 5 min each using ultrasonic treatment. To facilitate easy peeling from the glass substrate, a fluorinated polymer blended solution (Novec 1700:7100, 1:10 vol%, 3 M) was spin-coated onto the glass substrate at 2000 rpm (1 rpm = 2π per 60 rad s^{-1}) for 60 s, and a 1 μm-thick PaC film was deposited onto the surface of the fluorinated polymer/glass substrates through chemical vapor deposition. The 1 μm-thick PaC film was annealed at 120°C for 1 h. For PaC film planarization, a 500-nm-thick epoxy (SU-8 3005, MicroChem) layer was spin-coated at 5000 rpm for 60 s and pre-baked at 95°C for 2 min. Thereafter, the 500-nm-thick epoxy layer was annealed at 120°C for 1 h. Ultraflexible OECT devices were fabricated as described above for the prepared SU-8/PaC substrate.

7.4. Device characterization

Electrical characterization of 2-terminal (2-T) and 4-terminal (4-T) OECTs was performed using two source−measure-units (SMU) (Keithley 2400) under ambient conditions. All measurements were conducted in a 0.1 M NaCl aqueous solution, with an Ag/AgCl reference electrode immersed in 3 M KCl solution used as a gate electrode. Identical device geometries were employed for both 2-T and 4-T measurements, regardless of whether they were pOECT or vcOECT, except when the specific measurement conditions varied. The detailed measurement configuration is described in the Supporting Information Figure S10.

For 2-T measurements, the drain and source electrodes of the OECT devices were connected to the HI and LO terminals, respectively, of the SMUs for applying the drain voltage, with the drain current recorded by this unit. The Ag/AgCl gate electrode was connected to the HI terminal of another SMU to apply the gate voltage, and the ground of each SMU was shared by connecting both LO terminals to the OECT source electrode. The measurement mode for applying the drain current was set to the 2-wire mode using LabVIEW software.

For 4-T measurements, the connections for the source, drain, and gate electrodes were identical to those in the 2-T configuration. However, the voltage probes ($V_{Sense,1}$ and $V_{Sense,2}$) were connected to the 4-wire sense connector of the SMU, and the measurement mode was set to 4-wire sense mode using LabVIEW.

7.5. Electrocardiogram (ECG) signal measurement

To monitor ECG signals, an ultraflexible device was adhered to the right index finger using a drop of 0.1 M NaCl aqueous solution, with the source contact placed on the left chest via a gel electrode. The device pad was connected to an external wire with a Cr/Au (10/50 nm) line pattern, fabricated using the same method as in the stretchable vcOECT measurements. The end of the Au wire was connected to an alligator clip, which was attached to the gel electrode.

Note

Certain equipment, instruments, software, or materials are identified in this paper in order to specify the experimental procedure adequately. Such identification is not intended to imply recommendation or endorsement of any product or service by NIST, nor is it intended to imply that the materials or equipment identified are necessarily the best available for the purpose.

Code Availability

We provide the code utilized in this study to support public availability, which can be deposited in a public repository of *Materials Science and Engineering: R: Reports* journals.

CRediT authorship contribution statement

Flagg Lucas Q.: Writing – review & editing, Validation, Software, Investigation, Formal analysis, Data curation. **Mei Jianguo:** Writing – review & editing, Supervision, Project administration, Funding acquisition. **Kang Keehoon:** Writing – review & editing, Validation, Supervision, Project administration, Investigation. **You Liyan:** Validation, Data curation. **Chaudhary Jagrity:** Software, Investigation, Formal analysis, Data curation. **Lee Wonjune:** Writing – review & editing, Validation, Resources, Formal analysis, Data curation. **Lee Inho:** Writing – original draft, Validation, Software, Resources, Methodology, Data curation. **Kim Ji Hwan:** Writing – review & editing, Visualization, Methodology, Investigation, Formal analysis. **Park Sungjun:** Writing – review & editing, Validation, Supervision, Resources, Project administration, Funding acquisition, Conceptualization. **Lee Hyeongbeom:** Validation, Software, Methodology, Investigation, Formal analysis, Data curation. **Shin Dongjoon:** Visualization, Validation, Resources, Investigation, Formal analysis, Data curation, Conceptualization.

Declaration of Competing Interest

J. M. is a co-founder of Ambilight Inc., which partially sponsors the research under the research agreement.

Acknowledgments

W.-J.L., L.Y., and J.M. acknowledge the support from Ambilight Inc. under contract #4000187.02. J.C. was supported by the Multidisciplinary University Research Initiative (N00014–21–1–2476, Program Manager: Dr. Chad Stoltz). This research used beamline 11-BM (CMS) of National Synchrotron Light Source II, a US Department of Energy (DOE) Office of Science User Facility operated for the DOE Office of Science by Brookhaven National Laboratory under contract No. DE-SC0012704. This research was funded by the Ministry of Science and ICT (MSIT) (Grant No. IITP-2023–2020–0–01461, RS-2023–00213089, CRC23021–000, RS-2024–00403639, RS-2024–00403163). This research was funded by the Ministry of Trade, Industry and Energy (MOTIE) (Grant No. P0017805, RS-2022–00154781). This work was funded by the Ministry of Education (MOE) (Grant No. RS-2023–00220077).

Appendix A. Supporting information

Supplementary data associated with this article can be found in the online version at doi:10.1016/j.mser.2025.101003.

Data availability

Data will be made available on request.

References

[1] S. Park, S.W. Heo, W. Lee, D. Inoue, Z. Jiang, K. Yu, H. Jinno, D. Hashizume, M. Sekino, T. Yokota, K. Fukuda, K. Tajima, T. Someya, Nature 561 (2018) 516–521.
[2] W. Lee, S. Kobayashi, M. Nagase, Y. Jimbo, I. Saito, Y. Inoue, T. Yambe, M. Sekino, G.G. Malliaras, T. Yokota, M. Tanaka, T. Someya, Sci. Adv. 4 (2018) eaau2426.
[3] I. Lee, J.H. Kim, Y. Kim, D. Shin, H. Lee, J. Won, K. Kang, J.-G. Choi, M.-H. Yoon, S. Park, Adv. Mater. N./a (2024) 2410444.
[4] J. Rivnay, P. Leleux, M. Sessolo, D. Khodagholy, T. Hervé, M. Fiocchi, G. G. Malliaras, Adv. Mater. 25 (2013) 7010–7014.
[5] H. Liao, A. Savva, A.V. Marsh, Y.-Y. Yang, H. Faber, M. Rimmele, M. Sanviti, R. Zhou, A.-H. Emwas, J. Martín, T.D. Anthopoulos, M. Heeney, Angew. Chem. 137 (2025) e202416288.
[6] T. Yamane, D.C. Shah, P. Jaïs, M. élèze Hocini, I. Deisenhofer, K.-J. Choi, L. Macle, J. Clémenty, M. Haïssaguerre, J. Am. Coll. Cardiol. 39 (2002) 1337–1344.
[7] X. Wu, H. Tang, Z. Zhou, T. Salim, C.G. Tang, F. Huang, W.L. Leong, Chem. Mater. (2024).
[8] H. Tang, Y. Liang, C.-Y. Yang, X. Luo, J. Yu, K. Zhang, S. Fabiano, F. Huang, Mater. Horiz. (2024).
[9] Y. Liang, C. Che, H. Tang, K. Zhang, L. Lan, C. Zhou, Y. Ma, F. Huang, ACS Appl. Mater. Interfaces (2023).
[10] A. Giovannitti, C.B. Nielsen, D.-T. Sbircea, S. Inal, M. Donahue, M.R. Niazi, D. A. Hanifi, A. Amassian, G.G. Malliaras, J. Rivnay, I. McCulloch, Nat. Commun. 7 (2016) 13066.
[11] J. Baek, J.G. Oh, K. Lee, D. Kim, D. Lee, S.B. Kim, J. Jang, Adv. Funct. Mater. 35 (2025) 2414916.
[12] X. Peng, K. Dong, C. Ye, Y. Jiang, S. Zhai, R. Cheng, D. Liu, X. Gao, J. Wang, Z. L. Wang, Sci. Adv. 6 (2020) eaba9624.
[13] D. Lei, J. Wu, Y. Zi, C. Pan, H. Cui, X. Li, ACS Appl. Electron. Mater. 5 (2023) 2819–2828.
[14] W. Zhang, Y. Zhang, G. Yang, X. Hao, X. Lv, F. Wu, J. Liu, Y. Zhang, Nano Energy 82 (2021) 105769.
[15] Z. Ke, A. Abtahi, J. Hwang, K. Chen, J. Chaudhary, I. Song, K. Perera, L. You, K. N. Baustert, K.R. Graham, J. Mei, J. Am. Chem. Soc. 145 (2023) 3706–3715.
[16] Z. Ke, J. Chaudhary, L.Q. Flagg, K.N. Baustert, A.O. Yusuf, G. Liu, L. You, K. R. Graham, D.M. DeLongchamp, J. Mei, Adv. Funct. Mater. 34 (2024) 2400255.
[17] J.H. Kim, Z. Ahmad, Y. Kim, W. Kim, H. Ahn, J.-S. Lee, M.-H. Yoon, Chem. Mater. 32 (2020) 8606–8618.
[18] D. Jeong, I.-Y. Jo, S. Lee, J.H. Kim, Y. Kim, D. Kim, J.R. Reynolds, M.-H. Yoon, B. J. Kim, Adv. Funct. Mater. 32 (2022) 2111950.
[19] R. Halaksa, J.H. Kim, K.J. Thorley, P.A. Gilhooly-Finn, H. Ahn, A. Savva, M.-H. Yoon, C.B. Nielsen, Angew. Chem. Int. Ed. 62 (2023) e202304390.
[20] J.H. Kim, R. Halaksa, I.-Y. Jo, H. Ahn, P.A. Gilhooly-Finn, I. Lee, S. Park, C. B. Nielsen, M.-H. Yoon, Nat. Commun. 14 (2023) 7577.
[21] B. Wang, Y. Kong, S. Zhang, Z. Wu, S. Wang, J. Ren, H.Y. Woo, Y. Li, W. Ma, Adv. Funct. Mater. 34 (2024) 2312822.
[22] S. Griggs, A. Marks, H. Bristow, I. McCulloch, J. Mater. Chem. C. 9 (2021) 8099–8128.
[23] Y. Lu, J.-Y. Wang, J. Pei, Chem. Mater. 31 (2019) 6412–6423.
[24] B. Lüssem, C.-M. Keum, D. Kasemann, B. Naab, Z. Bao, K. Leo, Chem. Rev. 116 (2016) 13714–13751.
[25] X. Yan, M. Xiong, X.-Y. Deng, K.-K. Liu, J.-T. Li, X.-Q. Wang, S. Zhang, N. Prine, Z. Zhang, W. Huang, Y. Wang, J.-Y. Wang, X. Gu, S.K. So, J. Zhu, T. Lei, Nat. Commun. 12 (2021) 5723.
[26] X. Zheng, X. Jiang, W. Liu, C. Cao, N. Wei, Z. Wei, L. Zhang, H. Wu, A. Zhang, C. Li, Y. Liu, H. Lu, X. Xu, Z. Tang, Z. Bo, Angew. Chem. Int. Ed. 63 (2024) e202412854.
[27] J. Guo, L.Q. Flagg, D.K. Tran, S.E. Chen, R. Li, N.B. Kolhe, R. Giridharagopal, S. A. Jenekhe, L.J. Richter, D.S. Ginger, J. Am. Chem. Soc. 145 (2023) 1866–1876.
[28] X. Wu, Q. He, Z. Zhou, T.L.D. Tam, C. Tang, M. Lin, M. Moser, S. Griggs, A. Marks, S. Chen, J. Xu, I. McCulloch, W.L. Leong, Adv. Mater. 36 (2024) 2308823.
[29] Y. Wang, A. Koklu, Y. Zhong, T. Chang, K. Guo, C. Zhao, T.C.H. Castillo, Z. Bu, C. Xiao, W. Yue, W. Ma, S. Inal, Adv. Funct. Mater. 34 (2024) 2304103.
[30] Z. Huang, P. Li, Y. Lei, X.-Y. Deng, Y.-N. Chen, S. Tian, X. Pan, X. Lei, C. Song, Y. Zheng, J.-Y. Wang, Z. Zhang, T. Lei, Angew. Chem. 136 (2024) e202313260.
[31] W. Wu, K. Feng, Y. Wang, J. Wang, E. Huang, Y. Li, S.Y. Jeong, H.Y. Woo, K. Yang, X. Guo, Adv. Mater. 36 (2024) 2310503.
[32] S. Inal, G.G. Malliaras, J. Rivnay, Nat. Commun. 8 (2017) 1767.
[33] C. Cea, G.D. Spyropoulos, P. Jastrzebska-Perfect, J.J. Ferrero, J.N. Gelinas, D. Khodagholy, Nat. Mater. (2020) 1–8.
[34] J.T. Friedlein, R.R. McLeod, J. Rivnay, Org. Electron. 63 (2018) 398–414.
[35] M. Mori, A. Hamamoto, A. Takahashi, M. Nakano, N. Wakikawa, S. Tachibana, T. Ikehara, Y. Nakaya, M. Akutagawa, Y. Kinouchi, Med Bio Eng. Comput. 45 (2007) 1237–1241.

[36] R. Maiti, L.-C. Gerhardt, Z.S. Lee, R.A. Byers, D. Woods, J.A. Sanz-Herrera, S. E. Franklin, R. Lewis, S.J. Matcher, M.J. Carré, J. Mech. Behav. Biomed. Mater. 62 (2016) 556–569.
[37] A. Chortos, Z. Bao, Mater. Today 17 (2014) 321–331.
[38] J. Ilavsky, J. Appl. Cryst. 45 (2012) 324–328.
[39] A.D. Becke, Phys. Rev. A 38 (1988) 3098–3100.
[40] C. Lee, W. Yang, R.G. Parr, Phys. Rev. B 37 (1988) 785–789.
[41] W.J. Hehre, R.F. Stewart, J.A. Pople, J. Chem. Phys. 51 (1969) 2657–2664.
[42] A.V. Marenich, C.J. Cramer, D.G. Truhlar, J. Phys. Chem. B 113 (2009) 6378–6396.

Prof. Keehoon Kang is currently an assistant professor at Department of Materials Science and Engineering at Seoul National University, South Korea. He obtained his BA & MSci (combined) and PhD in Physics in 2012 and 2017, respectively, at University of Cambridge. After his postdoctoral research in Department of Physics at Seoul National University (military service), he transitioned to a faculty position in the Department of Materials Science and Engineering at Yonsei University from 2021 to 2022. Currently, at Seoul National University, he is leading ONELab (Organic Next-gen Electronics) and is actively focused on the cutting-edge fields of mixed-ionic-electronic conducting organic semiconductors and metal-halide perovskites. He is dedicated to exploring the fundamentals and new doping strategies for controlling electrical properties of these novel materials for next-generation electronics.

Prof. Jianguo Mei is currently Richard and Judith Wien Professor of Chemistry in Tarpo Department of Chemistry at Purdue University. He obtained his PhD degree from the University of Florida and received his Postdoc training at Stanford University. He joined Purdue University in 2014. His current research focuses on organic semiconductors and conductors and their applications in flexible electronics and bioelectronics. He cofounded Ambilight Inc - a leading company in electrochromic technologies.

Prof. Sungjun Park is an Associate Professor in the Department of Electrical and Computer Engineering and the Department of Intelligence Semiconductor Engineering at Ajou University, Republic of Korea. He earned his PhD in 2016 from the School of Materials Science and Engineering at the Gwangju Institute of Science and Technology, Republic of Korea. Before joining Ajou University in 2020, he conducted postdoctoral research at RIKEN in Japan and worked as a Senior Researcher at the Samsung Advanced Institute of Technology (SAIT) in the Republic of Korea. Prof. Park's research focuses on skin-conformal electronic materials, devices, and integration for wearable sensors and bioelectronics.